

1

2 **Parameterization and Evaluation of Nonhydrostatic Effect in the**
3 **Orographic Gravity Wave Drag in China Meteorological**
4 **Administration Global Forecast System (CMA-GFS) v4.0 Model**

5

6 Rongrong ZHANG^{1,2,3}, Zhenzhen AI¹, Xin XU¹, Haile XUE^{4,5}, Qiyong CHEN^{4,5}

7 ¹State Key Laboratory of Severe Weather Meteorological Science and Technology, Key
8 laboratory of Mesoscale Severe Weather/Ministry of Education, School of Atmospheric Sciences,
9 Nanjing University, Nanjing 210023, China

10 ²Jiangsu Meteorological Observatory, Jiangsu Meteorological Bureau, Nanjing 210000, China

11 ³Jiangsu Key Laboratory of Severe Storm Disaster Risk/Key Laboratory of Transportation
12 Meteorology of CMA, Nanjing 210000, China

13 ⁴State Key Laboratory of Severe Weather Meteorological Science and Technology, CMA Earth
14 System Modeling and Prediction Centre, Beijing 100081, China

15 ⁵Key Laboratory of Earth System Modeling and Prediction, China Meteorological
16 Administration, Beijing 100081, China

17

18 Correspondence: Xin Xu (xinxu@nju.edu.cn) and Haile Xue (xuehl@cma.cn)

19

20

Abstract

21

22

23

24

25

26

27

28

29

30

31

32

33

34

35

36

37

38

39

40

41

42

43

44

The China Meteorological Administration Global Forecast System (CMA-GFS) v4.0 model was upgraded to a higher resolution of 0.125° in May 2023. To be compatible with its fine resolution, the parameterization scheme of orographic gravity wave drag (OGWD) in CAM-GFS is revised herein by accounting for the nonhydrostatic effect (NHE) on the wave momentum flux of subgrid-scale orographic gravity waves. The performance of the revised OGWD scheme is then evaluated for the 10-day medium-range forecast in December 2023. Results show that the revised OGWD scheme can better capture the large-scale circulation in the Northern Hemisphere (NH), particularly in the high latitudes. The easterly (westerly) wind biases in the NH polar stratosphere (troposphere) are decreased. The underestimation of East Asia subtropical jet is also alleviated. Quantitative evaluation shows that the revised OGWD scheme reduces both the mean bias and root mean square error of 500-hPa geopotential height in the NH after the 6th forecast day, reaching 11.59% and 5.06%, respectively, by day 10. The decrease of easterly biases in the polar stratosphere is owing to the weakening of stratospheric zonal OGWD by the NHE. For the decrease of westerly biases in the NH polar troposphere, it is due to the fact that the enhanced stratospheric winds suppress the upward propagation of Rossby waves into the stratosphere, resulting in greater convergence of Eliassen-Palm flux in the mid-upper troposphere.

Keywords: orographic gravity wave drag, parameterization, global NWP medium-range forecast

45 **1. Introduction**

46 Orographic gravity wave drag (OGWD) is an important process in atmospheric
47 dynamics, arising from the interaction of airflow with complex terrain (Kim et al., 2003;
48 Teixeira, 2014). When airstream flows over mountains, it generates orographic gravity
49 waves (OGWs) which propagate vertically. As these waves break, they transfer
50 momentum from the surface to higher levels (Fritts and Alexander, 2003). This
51 momentum transfer plays a crucial role in driving the atmospheric circulation,
52 influencing both tropospheric and stratospheric dynamics (Alexander et al., 2010).

53 In numerical weather prediction (NWP) and climate models, the OGWD is
54 typically a subgrid-scale process which needs to be parameterized. Various OGWD
55 parameterization schemes have been developed over the past few decades (e.g., Palmer
56 et al., 1986; McFarlane, 1987; Kim and Arakawa, 1995; Lott and Miller, 1997; Scinocca
57 and McFarlane, 2000; Kim and Doyle, 2005) based on both linear and nonlinear OGW
58 dynamics. Their implementation has been shown to help alleviate the systematic biases
59 in both NWP and climate models, ranging from general circulation to regional climate
60 and weather (e.g., Kim, 2007; McLandress et al., 2012; Choi and Hong, 2015; Zhong
61 and Chen, 2015; Chen et al., 2016; Lu et al., 2020; Zhang et al., 2020; Li et al., 2023;
62 Xu et al., 2023; Wei et al., 2025).

63 While accurate representation of OGWD is essential for weather forecast and
64 climate simulation/projection, traditional OGWD parameterization schemes rely on the
65 assumption of hydrostatic balance which can significantly simplify the formulae of
66 OGW dynamics. This assumption is appropriate for coarse-resolution numerical models
67 where subgrid-scale OGWs are dominated by hydrostatic GWs as the dominant subgrid

68 “mountains” are large. However, as the model resolution increases, the hydrostatic
69 assumption becomes less valid because the subgrid-scale orography (SSO) becomes
70 smaller, so that the unresolved GWs have shorter wavelengths. In this situation, the
71 nonhydrostatic effects (NHEs) will exert remarkable influences on the subgrid-scale
72 OGWs. Compared with hydrostatic OGWs, nonhydrostatic OGWs experience stronger
73 horizontal dispersion of wave energy, which reduces wave amplitude and can suppress
74 wave breaking and momentum deposition into the mean flow (Smith, 1979; Klemp and
75 Durran, 1983; Zängl, 2003). These NHEs are thus critical for accurately representing
76 the dynamical impacts of subgrid-scale OGWs in high-resolution models, e.g., the
77 *state-of-the-art* global NWP models.

78 Recently, Xu et al. (2021) theoretically derived the analytical expressions for
79 the surface wave momentum flux (WMF) of nonhydrostatic OGWs generated by
80 idealized three-dimensional orography. They found that the degree of nonhydrostaticity
81 can be measured by a nondimensional parameter of Froude number which is equal to
82 the wind speed over the mountain half width and buoyancy frequency, i.e., the inverse
83 of the nondimensional half-width Na/U (e.g., Zängl, 2003). Physically, this parameter
84 represents the ratio between the period of buoyancy oscillation and the time for airflow
85 travelling through the mountain. The larger the horizontal Froude number, the more
86 important the NHE is. Based upon the theoretical study, Xu et al. (2023, 2024) revised
87 the OGWD parameterization scheme developed by Kim and Doyle (2005, hereafter
88 KD05) by accounting for the NHE on the surface WMF of upward-propagating OGWs.
89 Then the new OGWD scheme was implemented in the Model for Prediction Across
90 Scales (MPAS), which was shown to improve the seasonal simulation of the

91 stratospheric polar night jet and reduce the wet biases over the western Tibetan Plateau
92 in winter. Li et al. (2024) further evaluated the revised OGWD scheme in the Weather
93 Research and Forecasting (WRF) model for short-range forecast of Northeast China
94 cold vortices (NECVs). The underestimation of the NECV intensity (in terms of
95 minimum 500-hPa geopotential height) is alleviated as the NHE decreases the lower-
96 tropospheric OGWD.

97 The China Meteorological Administration Global Forecast System (CMA-GFS)
98 is a rename of the Global/Regional Assimilation and Prediction System (GRAPES)
99 developed in early 2000s (Shen et al., 2017). Operationally running at the CMA Earth
100 System Modeling and Prediction Center, the CMA-GFS was upgraded to a new version
101 of v4.0 in May 2023, with its horizontal resolution increasing from about 0.25° to 0.125°
102 (about 13 km), along with many other improvements in the model dynamics and physics
103 (Shen et al., 2023). For instance, the convective triggering function and quasi-
104 equilibrium closure conditions are improved to reduce biases in tropics and enhance
105 forecast skill of precipitation in East Asia. In CMA-GFS, three components of subgrid
106 scale orography effects have been implemented, i.e., the blocking-flow drag (BFD), the
107 OGWD and turbulent orographic form drag (TOFD). The TOFD scheme was
108 implemented CMA-GFS based on Beljaars et al. (2004) and Xue et al. (2011) and will
109 not be further discussed as it is not relevant to the NHE effect studied in this study. The
110 BFD component based on Lott and Millor (1997, hereafter LM97) and OGWD
111 component from Kim and Arakawa (1995, hereafter KA95) were implemented in CMA-
112 GFS similar to that in Alpert (2004) and was described in Chen et al. (2016). It is
113 noticed that in the existing implementation, nonhydrostatic effects are only partly reflected

114 through a Scorer-parameter-based partitioning of the momentum stress when the model
115 grid point is located downstream of the subgrid orography. However, the launch-level
116 surface WMF itself still follows the original hydrostatic KA95 formulation. In order to be
117 compatible with its high resolution, this hydrostatic OGWD parameterization scheme
118 needs to be upgraded to account for the NHE.

119 Note that the present study extends the evaluation of the nonhydrostatic OGWD
120 scheme in the MPAS model presented in Xu et al. (2024) by transitioning it into a
121 practical, operational NWP. Although Xu et al. (2024) demonstrated the beneficial
122 impact of the revised OGWD scheme for long-term, large-scale circulation simulations,
123 its performance and value within a state-of-the-art, high-resolution global forecasting
124 system performing routine medium-range forecasts had not been tested. This work
125 provides this critical assessment using the CMA-GFS v4.0 model, with a specific focus
126 on forecast skill improvements for several quantitative metrics. The primary advance
127 lies in evaluating the revised OGWD scheme in reducing systematic forecast biases on
128 timescales directly relevant to weather prediction (1-10 days). Therefore, this research
129 bridges the gap between parameterization development and operational implementation,
130 demonstrating the tangible benefits of incorporating nonhydrostatic effects to improve
131 medium-range weather forecasting accuracy.

132 The remainder of the paper is organized as follows. Section 2 firstly introduces
133 the revision of the OGWD parameterization scheme and then describes the setup of the
134 numerical experiments. Section 3 gives an overall evaluation for the medium-range
135 forecast of large-scale atmospheric circulation by the CMA-GFS model. The NHE

136 effects on parameterized OGWD and large-scale circulation are examined in section 4.
 137 Finally, the paper is summarized in section 5 along with discussions.

138

139 **2. OGWD parameterization scheme and numerical experiments**

140 a. Revision of the KA95 OGWD parameterization scheme

141 The KA95 OGWD considers various aspects of the SSO including its standard
 142 deviation (σ_h), orographic asymmetry (OA) and orographic convexity (OC). The
 143 surface WMF of OGWs is given by

$$144 \quad \tau_0 = \rho_0 E \frac{m}{\lambda_{eff}} G \frac{|\mathbf{V}_0|^3}{N_0}, \quad (1)$$

145 where

$$146 \quad E = (OA + 2)^{C_E \frac{Fr_0}{Fr_c}}, m = (1 + L_x)^{OA+1}, G = \frac{Fr_0^2}{Fr_0^2 + C_G OC^{-1}}, Fr_0 = \frac{\sigma_h N_L}{|\mathbf{V}_L|}. \quad (2)$$

147 The variables ρ_0 , $|\mathbf{V}_0|$ and N_0 are the low-level (from the surface to $2\sigma_h$) mean air
 148 density, horizontal wind speed and buoyancy frequency. The parameter m denotes the
 149 “number of mountains” within the grid cell, characterizing the total volume of SSO
 150 associated with the orography length (L_x). The coefficient λ_{eff} acts as a tunable
 151 parameter denoting the effective grid length. The transition function G is an
 152 enhancement factor for sharp mountains as OC is large. This scheme also considers the
 153 effects of low-level wave breaking and/or lee wave trapping through the factor E , which
 154 is a function of the shape and location of the SSO within the model grid cell (i.e., OA),
 155 and the flow nonlinearity (i.e., $Fr_0 = \frac{Nh_0}{U}$). The two empirical constants are set to $C_E =$
 156 0.8 and $C_G = 0.5$, which are obtained empirically through a series of numerical
 157 simulations conducted in Kim and Arakawa (1995).

158 The surface WMF is transported upward level by level until reaching the model
 159 top or critical level. At each model level, airflow instability is checked according to the
 160 hypothesis of wave saturation (Lindzen, 1981) and wave-breaking (Miller and Palmer,
 161 1986).

162 Once the subgrid-scale OGWs saturate and break, they will exert a body force
 163 on the mean flow through the deposition of wave momentum, namely,

$$164 \quad \frac{d\mathbf{V}(z)}{dt} = \frac{1}{\rho(z)} \frac{\partial \boldsymbol{\tau}(z)}{\partial z}. \quad (3)$$

165 where $\mathbf{V}(z)$ and $\boldsymbol{\tau}(z)$ are the mean flow velocity and the WMF at height z , respectively.
 166 Note that both the directions of $\mathbf{V}(z)$ and $\boldsymbol{\tau}(z)$ are parallel to the mean flow at the low
 167 level (i.e., \mathbf{V}_L). Readers are referred to KA95 for more details about the scheme.

168 The hydrostatic KA95 scheme above is revised by taking into account the NHE
 169 on the surface WMF of OGWs, i.e.,

$$170 \quad \tilde{\tau} = \tau_0 [1 + NHE(Fr)]. \quad (4)$$

171 $\tilde{\tau}$ represents the nonhydrostatic surface WMF, where the NHE correction depends only
 172 on the horizontal Froude number $Fr = \frac{|\mathbf{v}_0|}{N_0 L_x}$

$$173 \quad NHE(Fr) = -\frac{9}{8} Fr^2 + e^{-2Fr^{-1}} \left(-\frac{5}{4} Fr^{-2} - \frac{1}{2} Fr^{-1} + \frac{5}{4} + \frac{9}{4} Fr + \frac{9}{8} Fr^2 \right). \quad (5)$$

174 Eq. (5) is adopted from Xu et al. (2021) for three-dimensional isotropic terrain. Specifically,
 175 the nonhydrostatic correction is defined as the ratio of the analytically derived
 176 nonhydrostatic surface WMF to its hydrostatic counterpart, which yields an algebraic
 177 correction factor depending only on the horizontal Froude number. Note that the
 178 horizontal Froude number is different from the traditional Froude number Fr_0 above
 179 which measures the flow nonlinearity. While Xu et al. (2021) have derived the fully

180 NHE for anisotropic terrain, the expressions involve complicated integrals that are not
181 suitable for practical use in parameterization [cf. their Eqs. (14) to (17)]. Xu et al. (2021)
182 demonstrated that terrain anisotropy only has a very weak influence on the NHE, so the
183 expression of NHE for isotropic terrain, i.e., Eq. (5), is used because of simplicity, since
184 only algebraic manipulations are involved. This is in agreement with Xu et al. (2023,
185 2024) and Li et al. (2024).

186

187 b. Setup of numerical experiments

188 The CMA-GFSv4.0 dynamical core is based upon the nonhydrostatic and
189 shallow atmospheric governing equations in spherical polar coordinates with full
190 physics packages (Shen et al., 2020). It adopts a regular latitude-longitude grid of
191 $0.125^\circ \times 0.125^\circ$ with *C*-grid staggering. In the vertical, a terrain-following height-based
192 grid is utilized along with Charney-Phillips staggering. There are 87 vertical levels,
193 with the model top located at 73 km. For model physics, the Liu-Ma microphysics
194 scheme (Ma et al., 2018) is employed, along with the RRTMG longwave and shortwave
195 radiation schemes (Morcrette et al., 2008), the MRF planetary boundary layer scheme
196 (Chen et al. 2020; Hong and Pan 1996), the CoLM land surface model (Dai et al., 2003),
197 NSAS convection scheme (Han and Pan, 2011; Liu et al., 2015), the combined KA95
198 OGWD and LM97 FBD parameterization scheme (Chen et al., 2016), and modified
199 Beljaars's TOFD scheme (Xue et al., 2011).

200 In order to examine the impact of the revised OGWD scheme on the medium-
201 range forecast, two sets of numerical simulations (i.e., EXP_CTL and EXP_NHE) are
202 conducted with different OGWD parameterization schemes, using the original KA95

203 scheme and the revised nonhydrostatic one, respectively. Both experiments consist of 31
204 individual forecasts, each initialized at 00 UTC for the days from 1 to 31 December 2023.
205 Herein, a winter month is chosen because the OGWD, which is mainly located in the
206 Northern Hemisphere (NH) given the pronounced orography, is the strongest in this
207 season (e.g., Xu et al. 2020; Lu et al. 2024). In each experiment, the CMA-GFS model
208 is integrated for 10 days, i.e., medium-range forecast, with 6-hr output interval. The
209 model initial conditions are derived from the $0.25^\circ \times 0.25^\circ$ ECMWF Reanalysis v5 (ERA5)
210 dataset (Hersbach et al., 2020), which are also used as reference for the evaluation of the
211 CMA-GFS forecasts. Although the horizontal resolution of ERA5 is coarser than that of
212 the CMA-GFS v4.0 simulations, ERA5 is adopted here as the verification reference
213 because it is a dynamically consistent reanalysis constrained by a broad range of
214 assimilated observations. In this study, ERA5 is not used to resolve the non-hydrostatic
215 subgrid-scale orographic gravity waves themselves. Instead, it serves as a benchmark for
216 evaluating the large-scale circulation response and medium-range forecast skill associated
217 with the revised OGWD parameterization.

218

219 **3. Evaluation of the medium-range forecast**

220 *a. Atmospheric circulation*

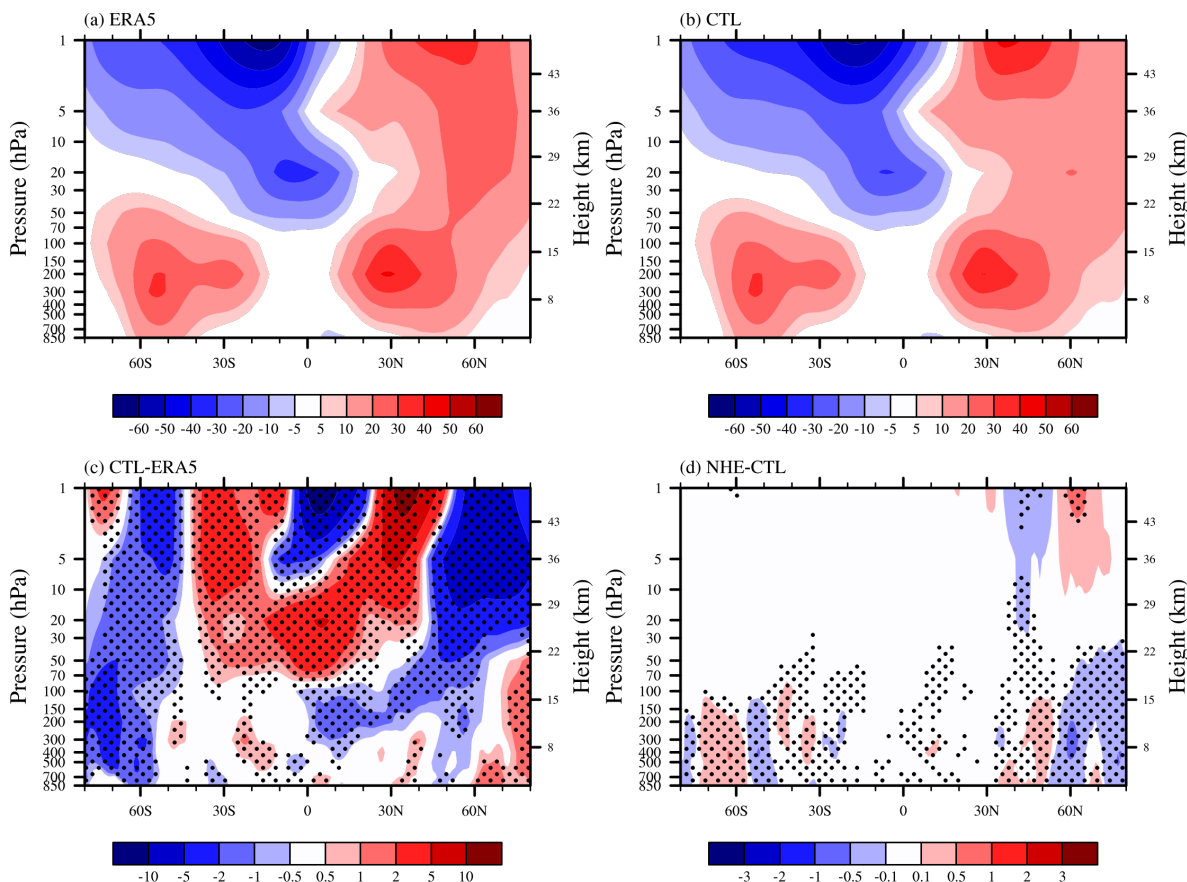
221 Figure 1 shows the zonal-mean zonal wind composited from the day 10 forecast
222 output of the 31 simulations initialized at 00 UTC on 1-31 December 2023. Accordingly,
223 the valid times of these day-10 forecasts span 10 December 2023 to 10 January 2024 (i.e.,
224 the 10th day of the medium-range forecast). In the winter of NH, as revealed by the
225 ERA5 reanalysis (Fig. 1a), there is a subtropical jet in the midlatitudes troposphere and

226 stratosphere, with the jet core located at about 200 hPa and 30°N. The maximum zonal
227 wind speed exceeds 35 m s^{-1} . In the stratosphere of high latitudes, there is another wind
228 maxima near 1 hPa and 60°N, which is the well-known polar-night jet (e.g., Kim, 2007)..
229 In the Southern Hemisphere (SH), which is in summer, there is also a upper tropospheric
230 lower stratospheric jet but relatively weaker and lower than in the NH. The SH jet core
231 is located at about 50°S, with a secondary one near 30°S. During austral summer, the
232 SH stratosphere is dominated by easterlies, which is distinctly different from the NH. With
233 a center located near 1 hPa and 20°S, the stratospheric easterlies extend downward and
234 equatorward to the tropics. An easterly jet of over -30 m s^{-1} can be found near 20 hPa
235 and 5°S.

236 Figure 1b is similar to Figure 1a but for the zonal-mean zonal winds obtained in
237 the EXP_CTL experiment. In general, the CMA-GFS model can capture the overall
238 pattern of the zonal-mean zonal winds, such as the tropospheric westerly jets in both
239 hemispheres and the easterly winds in the SH stratosphere. The polar night jet in the
240 NH, however, is underestimated by the model, with the jet core shifted southward by
241 about 10 latitudes. As shown in Fig. 1c, there are notable easterly biases of over -5 m
242 s^{-1} in the stratosphere of the NH high latitudes (north of 50°N). By contrast, westerly
243 biases are present in the upper stratosphere of the NH midlatitudes (25°N-50°N) which
244 can exceed 10 m s^{-1} , extending downward and equatorward to the lower stratosphere of
245 the tropics. Similarly, the zonal-mean zonal winds in the NH troposphere are
246 overestimated in the Arctic region, but with easterly biases in the mid-lower latitudes.
247 In the SH, the stratospheric easterlies are shifted northward, leading to westerly biases
248 in the mid-lower latitudes (40°S-5°S) and easterly biases in the tropics and lower

249 latitudes of the NH (5°S - 20°N). In the high latitudes, there are predominantly easterly
250 biases in both troposphere and stratosphere except in the upper stratosphere over the
251 polar cap.

252 When taking into account the NHE in the OGWD parameterization scheme, the
253 CMA-GFS model can better capture the large-scale circulation. Figure 1d presents the
254 differences between the zonal-mean zonal winds in the two numerical experiments (i.e.,
255 EXP_NHE minus EXP_CTL). In the stratosphere above ~ 10 hPa, positive and negative
256 wind differences are found to the north and south of 60°N , respectively, which are just
257 opposed to the wind biases in Figure 1c. It suggests that both the magnitude and location
258 of the polar night jet are improved. For example, the NH easterly biases in the mid-
259 upper stratosphere (~ 10 hPa to 1 hPa) are reduced by about 3%. The westerly biases in
260 the troposphere of Arctica region are also reduced, which reaches up to about 42% of
261 the total bias. At the same time, the easterly wind biases in the mid-latitude troposphere
262 have also reduced.



263

264 Figure 1. Vertical distributions of zonal-mean zonal wind (units: m s^{-1}) averaged in the
 265 period of 10 December 2023 to 10 January 2024 obtained from (a) ERA5 and (b)
 266 EXP_CTL, with their difference (i.e., EXP_CTL minus ERA5) given in (c). (d) is
 267 similar to (c) but for the difference between the two experiments of EXP_NHE and
 268 EXP_CTL (i.e., EXP_NHE minus EXP_CTL). Stippling in (c) and (d) denote
 269 differences statistically significant at the 95% confidence level.

270

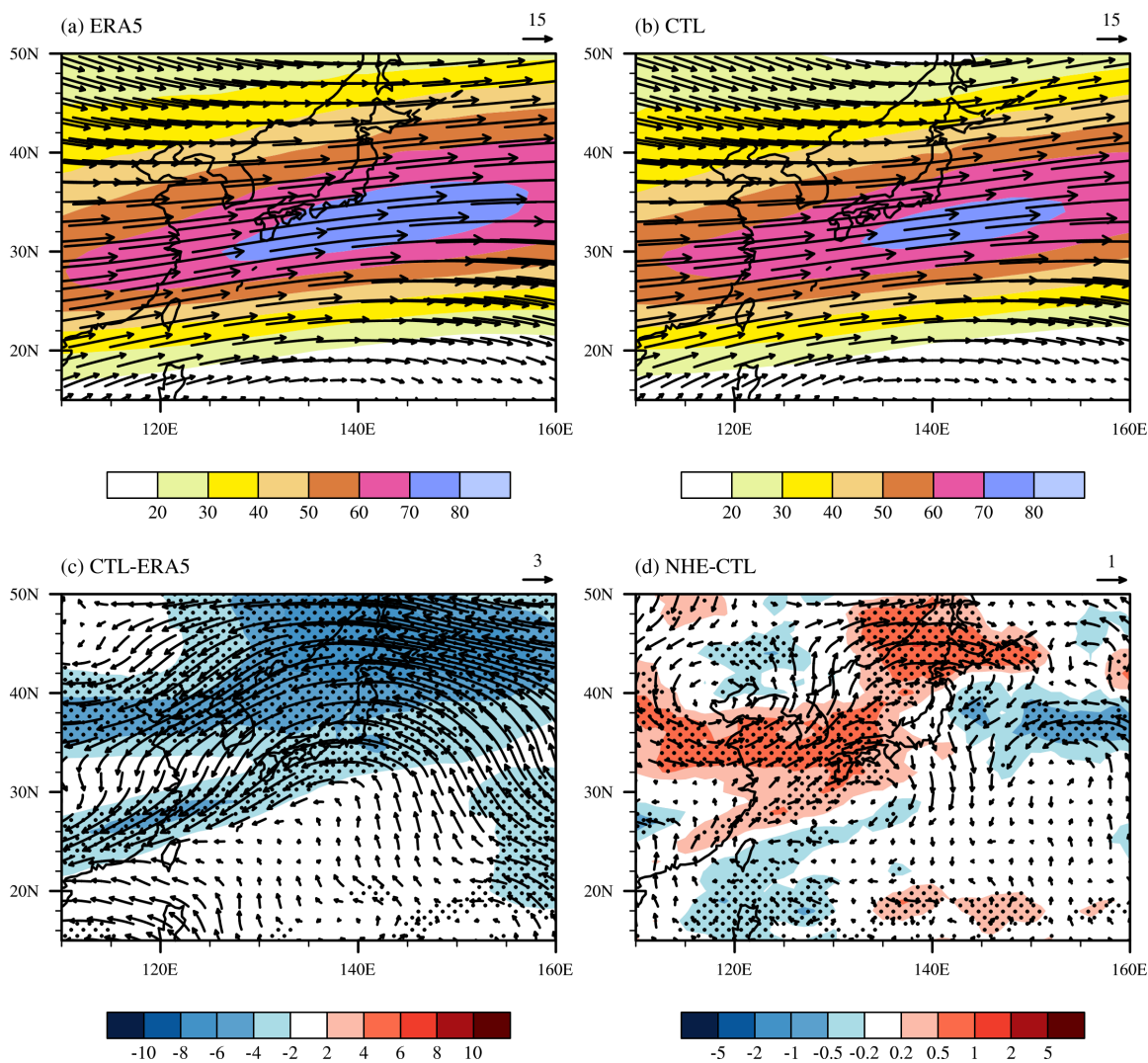
271 For the zonal-mean zonal wind biases in the SH stratosphere, they are hardly
 272 alleviated, however. This is because the stratospheric OGWD is very weak in summer
 273 (see Fig. 5a of Xu et al. 2024; see also Fig. 3 below), given the absorption of OGWs at
 274 the critical level (Booker and Bretherton, 1967), that is, the zero-wind level between
 275 the tropospheric westerlies and the stratospheric easterlies (Fig. 1a). The easterly biases
 276 in the troposphere of the high latitudes are reduced, especially around 60°S .

277 Although there is no significant improvement for the zonal-mean zonal wind in
278 the NH mid-lower latitudes (Fig. 1d), the wind circulation can be improved regionally,
279 such as the East Asia subtropical jet (EASJ). Figure 2a shows the horizontal wind field
280 and speed at 200 hPa averaged in the period of 10 December 2023 to 10 January 2024
281 from the ERA5 reanalysis. In boreal winter, the EASJ stretches from about 110°E to
282 160°E in the latitudes between about 25°N and 45°N. The jet core is located near Japan,
283 showing a high wind speed of over 70 m s⁻¹. The simulated EASJ in the EXP_CTL
284 experiment generally aligns well with the ERA5 reanalysis, in terms of its location and
285 orientation (Fig. 2b). But the jet intensity is underestimated, showing easterly biases of
286 over -4 m s⁻¹ (Fig. 2c). In the EXP_NHE experiment, the underestimation of the EASJ
287 is alleviated, with the mean bias decreased by about 6% (Fig. 2d).

288

289

290



291

292 Figure 2. Horizontal distributions of wind speed (shading; units: m s^{-1}) and wind field
 293 (arrow) at 200 hPa averaged in the period of 10 December 2023 to 10 January 2024
 294 obtained from (a) ERA5 and (b) EXP_CTL, with their difference (i.e., EXP_CTL minus
 295 ERA5) given in (c). (d) is similar to (c) but for the difference between the two
 296 experiments of EXP_NHE and EXP_CTL (i.e., EXP_NHE minus EXP_CTL).
 297 Stippling in (c) and (d) denote differences statistically significant at the 95% confidence
 298 level.

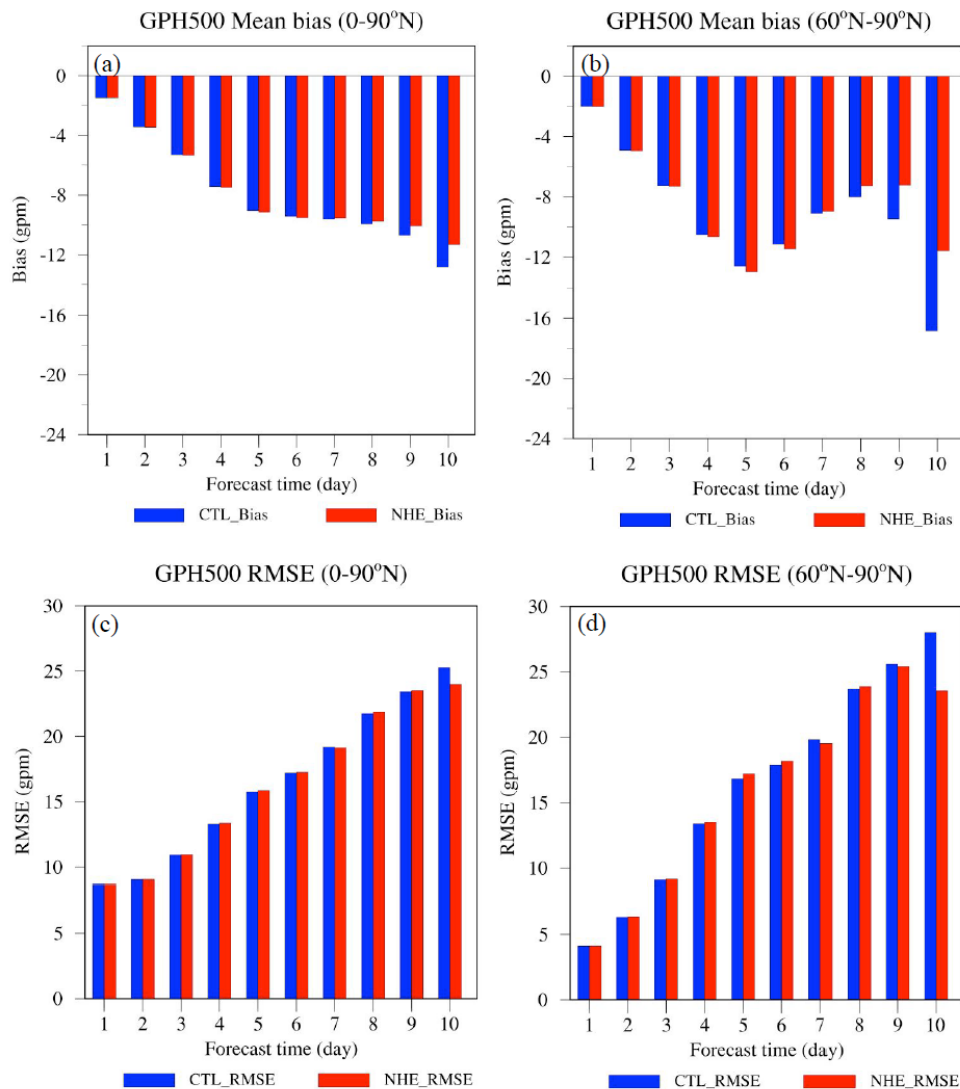
299

300

301

302 *b. Quantitative evaluation of forecast skills*

303 For medium-range forecast, the wind circulation in the troposphere is often of
 304 greater interest than in the stratosphere. To better evaluate the performance of the
 305 revised OGWD scheme, Figures 3a and 3b depict the mean bias (MB) and root mean
 306 square error (RMSE) for the 500 hPa geopotential height (GPH500) in the two
 307 experiments. Herein, we are interested in the NH because of the relatively weak wind
 308 differences in the SH (Fig. 1d) which is mainly covered by the ocean. Moreover, as will
 309 be shown below, the parameterized OGWD changes little in the SH.

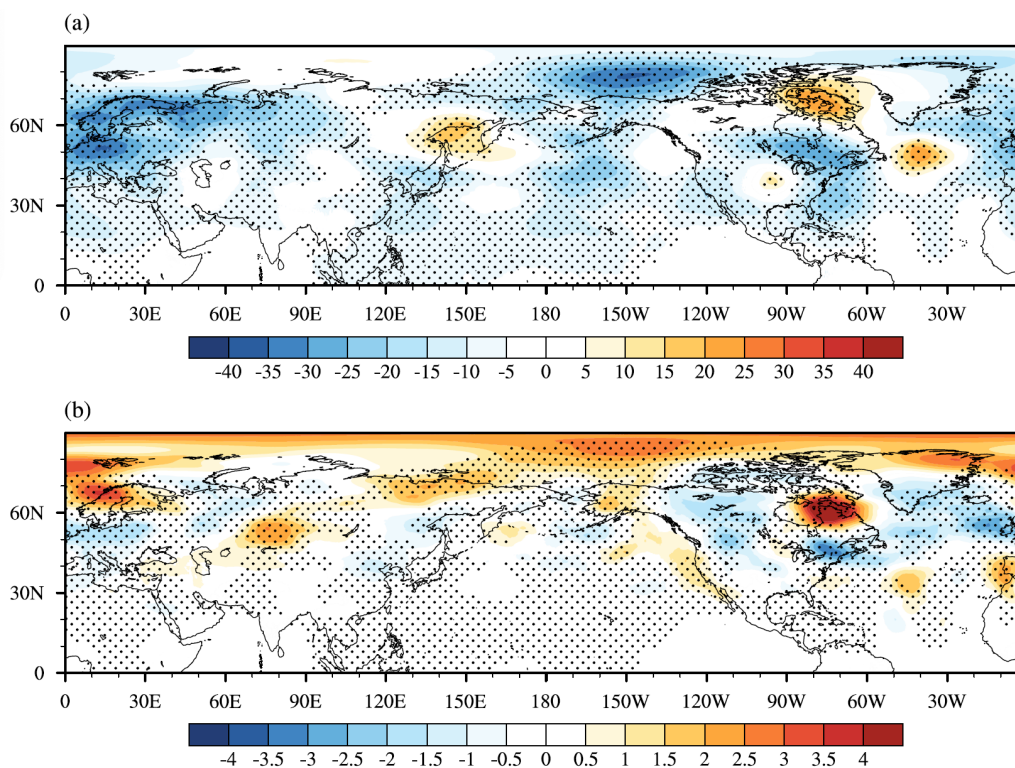


310

311 Figure 3. (a) Mean bias and (c) RMSE of the GPH500 in the NH at different forecast
312 lead time. (b) and (d) are similar to (a) and (c) but in the region north of 60°N.

313

314 In both experiments, the model GPH500 is lower than the ERA5 reanalysis, with
315 the MB and RMSE increasing with the forecast lead time (Figs. 3a, 3c). The GPH500
316 shows obvious underestimation in the EXP_CTL experiment which are significantly
317 reduced in EXP_NHE. This improvement is particularly evident in high latitudes north
318 of 60°N which is overall statistically significant at the 95% confidence level (Figs. 4a,
319 4b). Compared to EXP_CTL, EXP_NHE exhibits even greater MB and RMSE of
320 GPH500 till the 6th forecast day. Nevertheless, both the MB and RMSE of the GPH500
321 decrease quickly afterwards, which are reduced by 11.59% and 5.06%, respectively, at
322 the 10th day of the forecast (Table 1). Greater improvements are found for the GPH500
323 between 60°N and 90°N, the MB and RMSE of which are decreased by 31.18% and
324 15.93%, respectively, at the 10th forecast day (Table 1). All the values shown in Table
325 1 are statistically significant at the 95% confidence level. For the total 10 forecast days
326 as a whole, the MB and RMSE of GPH500 are separately reduced by 2.6% and 0.52 %,
327 indicating an overall improvement in the simulation of the large-scale circulation in the
328 NH when using the revised OGWD scheme (see Table 2).



329

330 Figure 4. (a) Mean biases of GPH500 (shading; units: gpm) in EXP_CTL experiment
 331 as compared to ERA5 averaged over the ten forecast days. (b) is similar to (a) but for
 332 the differences between the GPH500 (shading; units: gpm) in EXP_CTL and
 333 EXP_NHE experiments (i.e., EXP_NHE minus EXP_CTL). Stippling in (a) and (b)
 334 denote differences statistically significant at the 95% confidence level.

335

336 Table 1. Mean bias and RMSE of the 500-hPa geopotential height (GPH500) and sea
 337 level pressure (SLP) at the 10th forecast day

	Region	Mean Bias			RMSE		
		CTL	NHE	$\frac{NHE - CTL}{CTL} \times 100$	CTL	NHE	$\frac{NHE - CTL}{CTL} \times 100$
GPH500 (gpm)	0-90°N	-12.825	-11.338	-11.59	25.263	23.984	-5.06
	60°N-90°N	-16.841	-11.590	-31.18	28.017	23.554	-15.93
SLP (hPa)	0-90°N	-0.522	-0.343	-34.29	2.714	2.515	-8.33
	60°N-90°N	-1.712	-1.079	-36.97	3.049	2.517	-17.45

338

339 Table 2. Mean bias and RMSE of the 500-hPa geopotential height (GPH500) and sea
 340 level pressure (SLP) for the overall ten forecast days

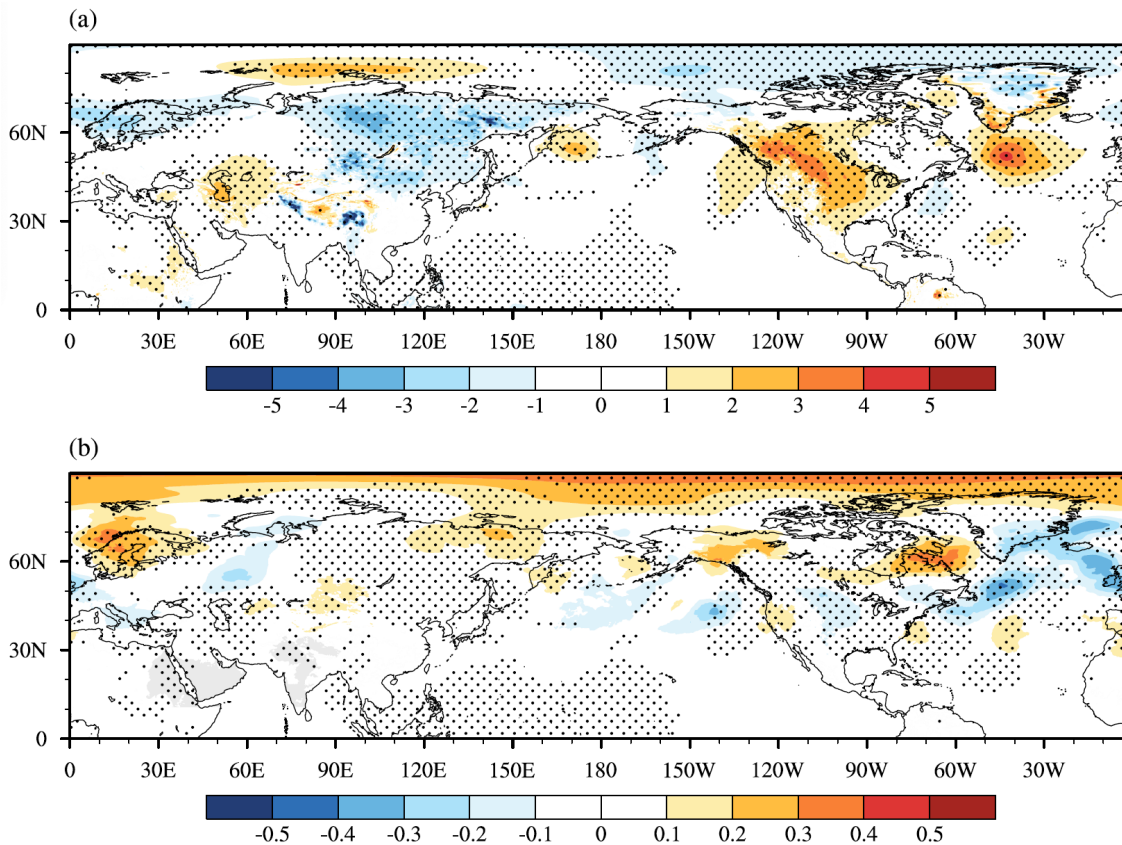
		Mean Bias			RMSE		
	Region	CTL	NHE	$\frac{NHE - CTL}{CTL} \times 100$	CTL	NHE	$\frac{NHE - CTL}{CTL} \times 100$
GPH500 (gpm)	0-90°N	-7.923	-7.717	-2.6	16.455	16.369	-0.52
	60°N-90°N	-9.187	-8.438	-8.15	16.470	16.089	-2.31
SLP (hPa)	0-90°N	-0.107	-0.082	-23.46	1.87	1.841	-1.53
	60°N-90°N	-0.498	-0.411	-17.47	1.598	1.532	-4.13

341

342 Besides the GPH500, the forecast skill is also examined for the SLP in the NH.
 343 As shown in Fig. 5a, the EXP_CTL experiment systematically underestimates the SLP
 344 over East Asia and the Arctic, while overestimating SLP across North America and the
 345 northern Atlantic. These biases are substantially corrected in the EXP_NHE experiment,
 346 particularly in high-latitude regions north of 60°N (Fig. 5b). Similarly, the EXP_NHE
 347 experiment firstly experiences a degradation in the early 6 days compared to EXP_CTL,
 348 but it shows significant improvement at the end of the 10th forecast day, with the MB
 349 reduced by 34.29% and the RMSE by 8.33%, respectively (Table 1). Greater decreases
 350 of 36.97% (for MB) and 17.45% (for RMSE) are found in the high latitudes north of
 351 60°N as well.

352

353



354

355 Figure 5. (a) Mean biases of SLP (shading; units: hPa) in the EXP_CTL experiment as
 356 compared to ERA5 averaged over the ten forecast days. (b) is similar to (a) but for the
 357 differences between the SLP (shading; units: hPa) in the EXP_CTL and EXP_NHE
 358 experiments (i.e., EXP_NHE minus EXP_CTL). Stippling in (a) and (b) denote
 359 differences statistically significant at the 95% confidence level.

360

361 From the above analyses, implementing the revised OGWD scheme in the high-
 362 resolution CMA-GFS model can help improve the medium range forecast of the NH
 363 large-scale circulation, especially in the high latitudes. In the next section, we will
 364 examine the underlying mechanisms responsible for the improvement of the circulation.

365

366

367 **4. Physical interpretation**

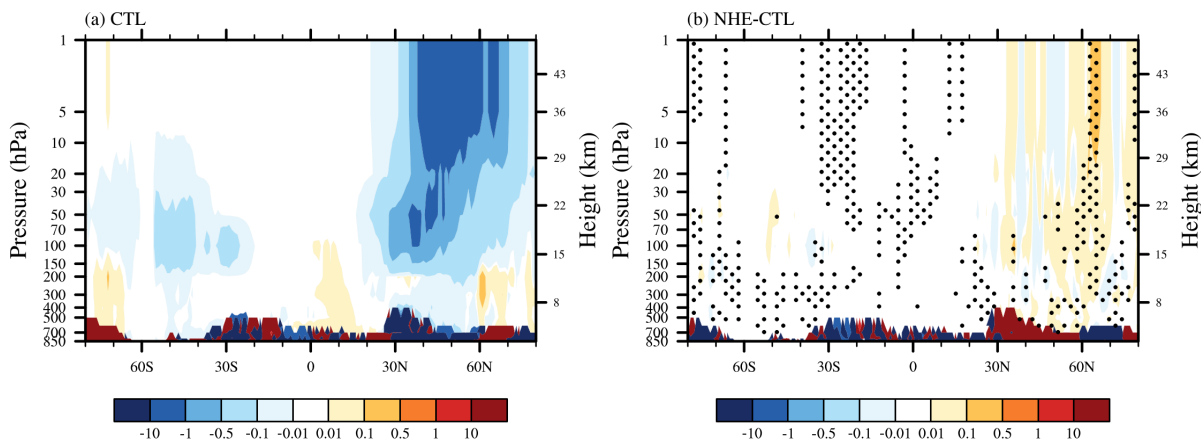
368 *a. Changes of parameterized OGWD*

369 The changes of wind circulation arise from the revision of the OGWD scheme.
370 It is thus straightforward to study the parameterized OGWD in these two experiments.
371 Figure 6a shows the vertical distribution of zonal-mean zonal OGWD averaged in the
372 period of 10 December 2023 to 10 January 2024 in the EXP_CTL experiment. The
373 differences between the parameterized OGWD in the two experiments (i.e., EXP_NHE
374 minus EXP_CTL) are given in Fig. 6b. In boreal winter, there exists prominent OGWD
375 in the stratosphere of the NH mid-to-high latitudes, which is favored by the decrease of
376 air density with height (e.g., Lindzen, 1981) and the relatively weak winds between the
377 tropospheric jet and polar night jet. The latter is called as the “valve layer” by Kruse et
378 al. (2016). The maximum OGWD occurs between about 20 hPa and 1 hPa. In contrast,
379 there is very weak OGWD in the SH stratosphere owing to the critical level absorption
380 as mentioned above.

381 Compared to that in EXP_CTL, the zonal-mean zonal OGWD in EXP_NHE is
382 generally weakened in the high latitudes of the NH (north of about 55°N), especially in
383 the stratosphere (Fig. 6b). Note that the positive difference indicates a decrease of
384 OGWD as the drag itself is negative. This is due to the fact that the NHE acts to decrease
385 the surface WMF [see Eqs. (4) and (5)], i.e., the source of parameterized OGWs which
386 determines the maximum wave momentum that can be deposited into the mean flow.
387 Therefore, the decrease of surface WMF is prone to reduce the OGWD. Note that there
388 is also enhancement of OGWD, e.g., in the stratosphere near 50°N. This may be
389 attributed to a decrease in surface WMF, which suppresses tropospheric wave breaking

390 by lowering the gravity-wave amplitude limit for breaking at lower levels and thus
 391 shifts the wave-breaking altitude upward. Consequently, a vertical structure
 392 characterized by alternating positive-negative-positive anomalies from the surface to
 393 the stratosphere would be expected. In consequence, more WMF is transported to the
 394 stratosphere where the OGWs break owing to the decay of air density and lead to
 395 stronger OGWD. This is similar to the redistribution of WMF in the vertical owing to
 396 selective critical level filtering of OGWs in directional shear flows (Shutts, 1995; Xu
 397 et al., 2012, 2019; van Niekerk et al., 2023). Generally, the changes in the vertical
 398 structure of parameterized OGWD in the CMA-GFS model are similar to that in the
 399 MPAS seasonal simulations conducted in Xu et al. (2024) which also considers the
 400 NHE correction to the OGWD (cf. their Fig. 5).

401



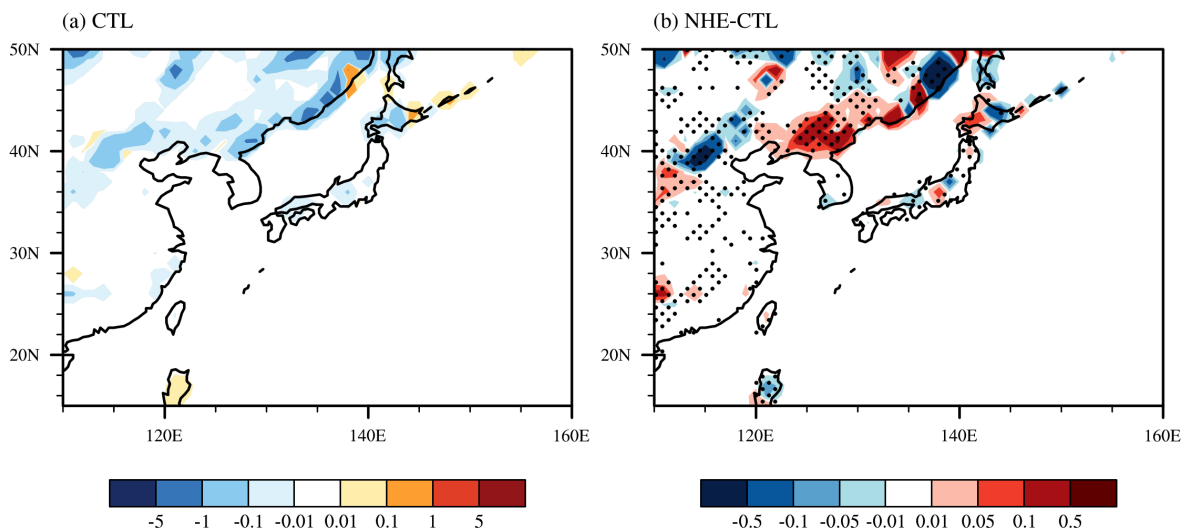
402

403 Figure 6. Vertical distributions of (a) zonal-mean zonal OGWD (units: $\text{m s}^{-1} \text{ day}^{-1}$)
 404 averaged in the period of 10 December 2023 to 10 January 2024 obtained from
 405 EXP_CTL, and (b) zonal-mean OGWD difference between the two experiments of
 406 EXP_NHE and EXP_CTL (i.e., EXP_NHE minus EXP_CTL). Stippling in (b) denotes
 407 differences statistically significant at the 95% confidence level.

408

409 The weakening of OGWD can directly increase the zonal winds in the polar
 410 stratosphere and the mid-latitude troposphere of the NH, thus leading to a recover of
 411 the weakened westerly jet. Conversely, the enhancement of OGWD can directly weaken
 412 the zonal winds in the mid-latitude stratosphere and the polar troposphere of the NH,
 413 thereby reducing the westerly biases (Figs. 1c, 1d). The parameterized OGWD in East
 414 Asia is also examined to explain the changes of EASJ. As shown in Fig. 7a, there is
 415 notable westward OGWD at 200 hPa in the high latitudes of East Asia where the
 416 underlying terrain is very complex, such as the Taihang, Yanshan, Changbai, Greater
 417 Khingan and Lesser Khingan Mountains. Thus, the largest easterly biases of the EASJ
 418 occur in this region (Fig. 2c). When accounting for the NHE in the OGWD
 419 parameterization scheme, the 200-hPa OGWD is mainly reduced (Fig. 7b). Clearly, the
 420 enhanced EASJ is owing to the weakening of the parameterized OGWD.

421



422

423 Figure 7. Horizontal distributions of (a) zonal OGWD (units: $\text{m s}^{-1} \text{ day}^{-1}$) at 200 hPa
 424 averaged in the period of 10 December 2023 to 10 January 2024 obtained from
 425 EXP_CTL, and (b) zonal OGWD difference between the two experiments of EXP_NHE

426 and EXP_CTL (i.e., EXP_NHE minus EXP_CTL) at 200 hPa. Stippling in (b) denotes
427 differences statistically significant at the 95% confidence level.

428

429 *b. Resolved Rossby-wave adjustment*

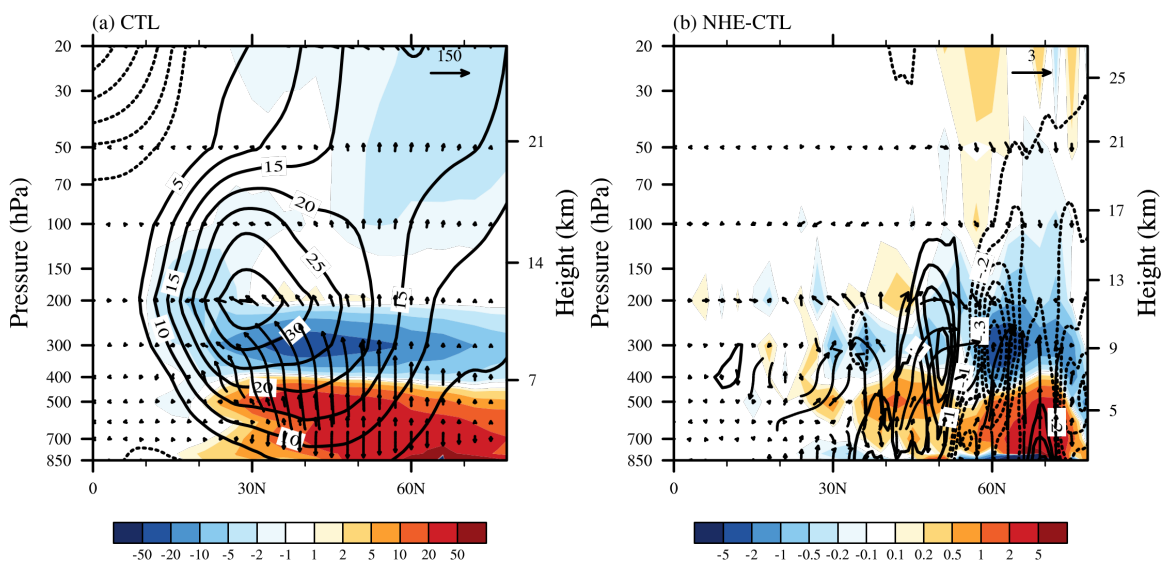
430 In addition to the direct effect of the modified OGWD, the tropospheric response
431 in the Northern Hemisphere is also associated with an adjustment of resolved large-scale
432 Rossby waves. This interpretation is consistent with the wave-drag compensation and
433 propagation-adjustment mechanisms discussed in previous studies (e.g., Cohen et al., 2013;
434 Sigmund and Shepherd, 2014). In particular, changes in the background zonal wind may
435 alter the propagation conditions for planetary waves and thereby redistribute the resolved
436 wave forcing between the troposphere and stratosphere.

437 It is well known that the impacts of large-scale Rossby waves on the mean flow
438 can be measured by the convergence of the zonal-mean Eliassen-Palm (EP) flux. Figure
439 8a illustrates the distribution of the zonal-mean EP flux in the EXP_CTL experiment
440 which is calculated following Edmon et al. (1980). In the NH middle-to-high latitudes,
441 Rossby waves originate from the lower troposphere which propagate upward and
442 converge in the upper troposphere. These waves split into two branches in the lower
443 stratosphere. The first branch turns to propagate equatorward across the tropospheric
444 jet. The other branch continues to propagate upward to the upper stratosphere where
445 the EP flux is converged and decelerates the mean flow. As in the SH, the Rossby waves
446 cannot propagate into the stratosphere (not shown) because of the presence of easterlies
447 there during austral summer (Fig. 1a).

448 Figure 8b is similar to Fig. 8a but gives the differences between the zonal-mean
449 EP fluxes in the two experiments (i.e., EXP_NHE minus EXP_CTL). Compared to

450 EXP_CTL, the upward propagation of Rossby waves into the stratosphere is suppressed
 451 in the high latitudes of the NH, leading to an enhanced convergence of EP flux in the
 452 troposphere. As a result, the zonal-mean zonal winds in the NH polar troposphere are
 453 decelerated by the large-scale Rossby wave forcing, which contributes to the alleviation
 454 of westerly biases there (Figs. 1c, 1d). This may explain why the improvements in the
 455 GPH 500 forecast emerge after 6 days in EXP_NHE (Fig. 2). The Rossby waves and
 456 their interaction with the mean flow require several days to develop fully and influence
 457 the large-scale circulation.

458



459

460 Figure 8. Vertical distributions of zonal-mean EP flux (vectors) and its divergence
 461 (shading; $\text{m s}^{-1} \text{ day}^{-1}$) due to resolved waves averaged in the period of 10 December
 462 2023 to 10 January 2024 obtained from (a) EXP_CTL, and (b) the difference between
 463 the two experiments of EXP_NHE and EXP_CTL (i.e., EXP_NHE minus EXP_CTL).
 464 Contours are the corresponding zonal-mean zonal wind (units: m s^{-1}).

465

466 The suppressed upward propagation of Rossby waves can be understood from
 467 the changes of the refractive index (*RFI*) that measures the ability of Rossby wave
 468 propagation (e.g., Chen and Robinson, 1992; Hu et al., 2019), which is defined as

$$469 \quad RFI = \left[\frac{\overline{q_\varphi}}{r\overline{U}} - \left(\frac{k}{r\cos\varphi} \right)^2 - \left(\frac{f}{2NH} \right)^2 \right] r^2, \quad (6)$$

470 where \overline{U} , k and H are the resolved zonal-mean zonal wind, zonal wave number and density
 471 scale height, respectively. $\overline{q_\varphi}$ represents the meridional gradient of the potential vorticity,
 472 which is expressed in the following form of

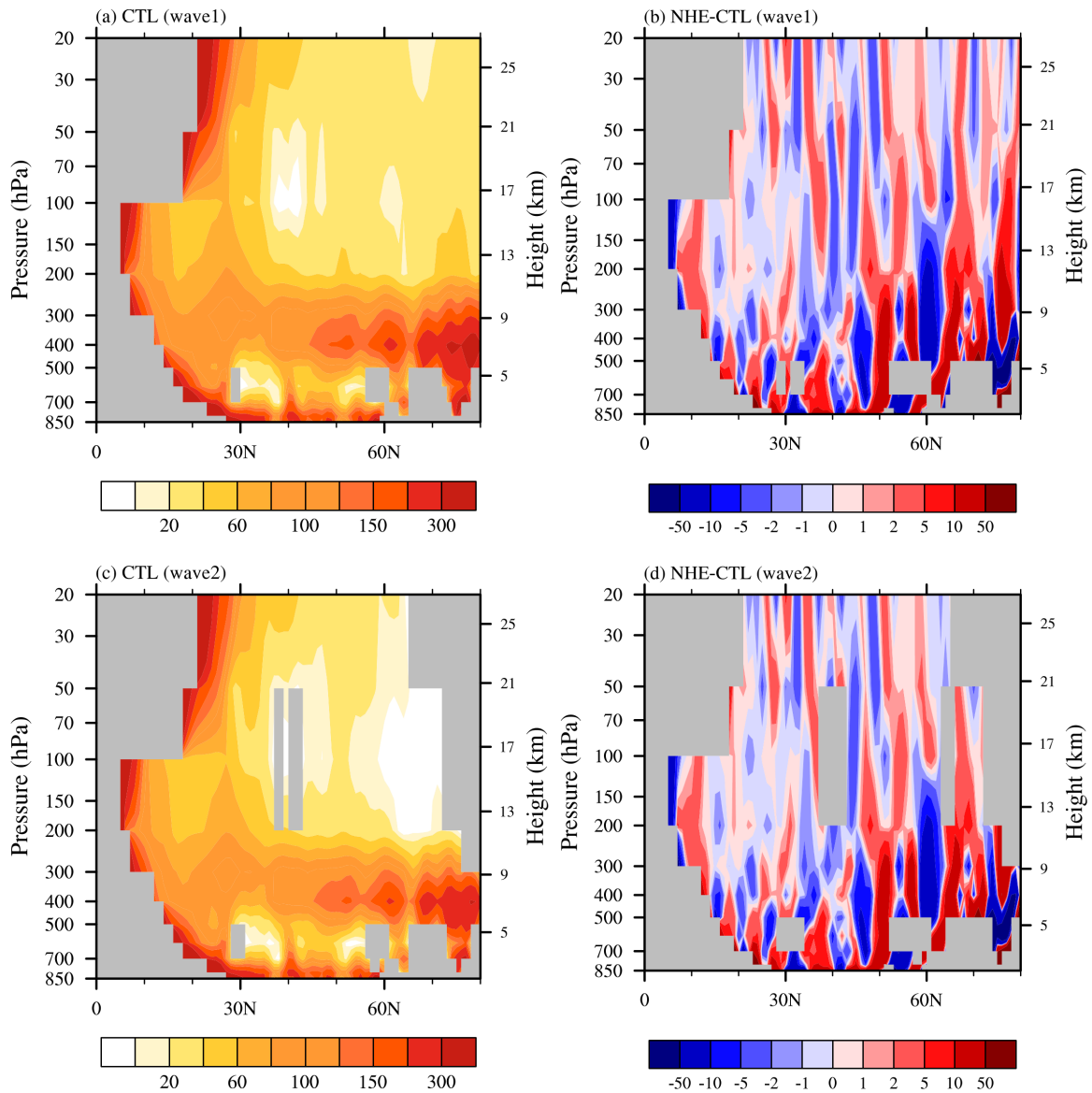
$$473 \quad \overline{q_\varphi} = 2\Omega\cos\varphi - \left[\frac{(\overline{U}\cos\varphi)_\varphi}{a\cos\varphi} \right]_\varphi + \frac{af^2}{R_d} \left(\frac{p\theta}{T} \frac{\overline{U}_p}{\theta_p} \right)_p. \quad (7)$$

474 where Ω , θ and R_d being the Earth's angular frequency, potential temperature and
 475 dry gas constant, respectively. The subscripts φ and p represent the partial derivatives with
 476 respect to latitude and pressure, respectively. The overbars indicate temporal and zonal
 477 averages. From Eq. (6), the increase of zonal wind will narrow the range of Rossby
 478 wave numbers that can propagate into the stratosphere (Charney and Drazin, 1961; Xu
 479 et al., 2024).

480 As shown in Fig. 9, positive *RFI* values for both zonal wavenumbers 1 and 2 are
 481 found over the northern mid- to high latitudes in EXP_CTL, indicating that the basic-
 482 state flow is favorable for the upward propagation of planetary waves (Figs. 9a, 9c).
 483 In EXP_NHE, however, the *RFI* is generally reduced over the same region, especially
 484 in the upper troposphere and lower stratosphere. These negative *RFI* anomalies suggest
 485 that the strengthened background westerlies in the polar stratosphere make the

486 environment less conducive to the vertical propagation of Rossby waves (Figs. 9b, 9d).
487 Similar behavior is found for both wavenumber-1 and wavenumber-2 components,
488 although the wavenumber-1 signal appears more spatially coherent. Therefore, the
489 reduction of *RFI* provides a dynamical explanation for the weakened upward EP-flux
490 branch seen in Fig. 8b.

491 Physically, the revised OGWD scheme weakens the parameterized drag in the
492 northern polar stratosphere, which strengthens the local westerlies. Stronger
493 background westerlies narrow the range of planetary-wave numbers that can propagate
494 vertically into the stratosphere. Consequently, the upward propagation of resolved
495 Rossby waves is suppressed, and less resolved wave forcing reaches the polar
496 stratosphere. This effect acts together with the weakened parameterized OGWD to
497 reduce the easterly wind bias in the polar stratosphere. At the same time, the associated
498 redistribution of resolved wave forcing favors a weakening of the polar-tropospheric
499 westerlies, thereby contributing to the improvement of the large-scale circulation over
500 the northern high latitudes.



501

502 Figure 9. Refractive index for the (a) wavenumber-1 and (c) wavenumber-2 resolved
 503 waves averaged over the period of 10 December 2023 to 10 January 2024 in the
 504 EXP_CTL experiment. (b) The difference between the refractive indices of
 505 wavenumber 1 in EXP_NHE and EXP_CTL (EXP_NHE minus EXP_CTL). (d) As in
 506 (b), but for wavenumber 2.

507

508

509

510 4. Summary and discussions

511 The latest China Meteorological Administration Global Forecast System (CMA-
512 GFS) v4.0 model has been upgraded to a higher resolution of 0.125° in 2023. However,
513 this high-resolution global model still uses the parameterization scheme of orographic
514 gravity wave drag (OGWD) developed by Kim and Arakawa (1995; KA95) which is
515 based on hydrostatic orographic gravity wave (OGW) theory. In this study, the KA95
516 OGWD scheme is revised by taking into account the nonhydrostatic effect (NHE) on
517 the surface wave momentum flux (WMF) of OGWs, according to the nonhydrostatic
518 OGW theory derived in our earlier study of Xu et al. (2021). The performance of the
519 revised OGWD scheme is then evaluated for the medium-range forecast of the CMA-
520 GFSv4.0 model. Two sets of numerical experiments (i.e., EXP_CTL and EXP_NHE)
521 are conducted by using the original KA95 scheme and the revised NHE scheme,
522 respectively. In each numerical experiment, there are in total 31 forecasts of 10-day
523 forecasts. In each numerical experiment, there are in total 31 independent 10-day
524 forecasts which are initiated at 00 UTC on each day of December 2023.

525 The results show that the revised OGWD scheme can improve the medium-
526 range forecast of large-scale circulation in the Northern Hemisphere (NH), especially
527 in the high latitudes. The easterly biases of zonal-mean zonal wind in the NH
528 stratosphere are reduced, with both the magnitude and location of the polar night jet
529 being better captured. The underestimation of the East Asia subtropical jet (EASJ) is
530 also alleviated. In contrast, the revised OGWD scheme shows little influence on the
531 stratospheric circulation in the Southern Hemisphere (SH). This is because, in boreal
532 winter (i.e., austral summer), there is hardly OGWD in the SH stratosphere owing to

533 the effect of critical-level absorption, leading to comparatively smaller circulation
534 responses. Therefore, the quantitative evaluation of forecast skill is mainly performed
535 for the NH, where the impact of the revised OGWD scheme is physically more
536 pronounced and statistically more robust.

537 Quantitative evaluation is performed for the medium-range forecast skills in the
538 NH, taking the ERA5 reanalysis dataset as reference. Both experiments showed lower
539 geopotential height (GPH) at 500 hPa than ERA5 reanalysis, with the mean bias (MB)
540 and root mean square error (RMSE) increasing with forecast lead time. EXP_NHE
541 initially has greater MB and RMSE than EXP_CTL until the 6th forecast day, but these
542 metrics decrease more rapidly afterwards, resulting in an 11.59% reduction in MB and
543 a 5.06% reduction in RMSE by day 10. Over the total 10 forecast days, the MB and
544 RMSE of the GPH 500 in the NH are reduced by 2.6% and 0.52%, respectively,
545 indicating improved simulation of large-scale circulation in the NH. The improvement
546 is more noticeable in the high latitudes north of about 60°N, where the MB and RMSE
547 of GPH 500 are decreased by 31.18% and 15.93% at the 10th forecast day. Similar
548 results are found for the sea level pressure (SLP) in the NH, the MB and RMSE of
549 which are reduced by 34.29% and 8.33%, respectively, by day 10 in EXP_NHE.

550 The dynamics responsible for the improvement of large-scale wind circulation are
551 examined. The NHEs act to decrease the surface WMF of OGWs, which leads to a general
552 weakening of the parameterized OGWD in the midlatitudes and high latitudes of the NH.
553 This weakening of OGWD directly increases the zonal winds in the mid-latitude
554 troposphere and polar stratosphere, reducing the easterly biases. The enhanced zonal wind
555 in the polar stratosphere acts to narrow the range of large-scale Rossby wave numbers

556 that can propagate into the stratosphere by reducing the refractive index of Rossby waves.
557 The suppressed upward propagation of Rossby waves leads to greater convergence of
558 Eliassen-Palm (EP) flux (i.e., resolved wave forcing) in the NH polar troposphere, which
559 decelerates the zonal winds and thus alleviates the westerly biases there.

560 To sum up, this study demonstrates that incorporating the NHE into the OGWD
561 parameterization scheme can help improve the simulation of large-scale atmospheric
562 circulation in high-resolution global NWP models, which is thus important for accurate
563 weather forecasts and/or climate simulations. However, there are still some limitations in
564 this work. For example, this study pays much attention to the medium-range forecast of
565 large-scale circulation in winter of NH. To further validate its effectiveness and robustness,
566 it is necessary to conduct more comprehensive evaluations of the nonhydrostatic OGWD
567 scheme in various numerical models focusing on different weather and climate systems.
568 Additionally, this work only takes into account the effects of NHE on the OGWD. Other
569 factors such as the vertical wind shear could also greatly affect the OGWD (e.g., Xu et al.,
570 2019; Xu et al., 2020; Zhang et al., 2025). While Xu et al. (2021) explored the
571 nonhydrostatic OGWs generated in a constant flow, it remains unclear how the vertical
572 wind shear affects the behavior of nonhydrostatic OGWs which needs further study.

573

574 *Code and data availability.* The China Meteorological Administration Global Forecast
575 System (CMA-GFS) model is archived on Zenodo under
576 <https://doi.org/10.5281/zenodo.18476721> (Zhang, 2026). The CMA-GFS outputs and the
577 ERA5 reanalysis data used for the comparison, along with the codes for orographic gravity
578 wave scheme are uploaded to <https://doi.org/10.5281/zenodo.18529537> (Zhang, 2026).

579
580 *Author contributions.* RRZ was responsible for formal analysis, writing the original draft
581 and visualization. ZZA carried out data analyses. XX developed the code and conducted
582 the analysis. HLX and QYC provided the resources and data curation.

583

584 *Competing interests.* The contact author has declared that none of the authors has any
585 competing interests.

586

587 *Acknowledgements.* The authors would like to express their sincere thanks to the
588 anonymous referees.

589

590 *Financial support.* This work is mainly supported by the National Natural Science
591 Foundation of China (grants no. U2342226, 42275163), the Joint Research Project for
592 Meteorological Capacity Improvement (grant no. 22NLTSZ006), and Jiangsu
593 Meteorological Observatory (grant no. KQ202502).

594

595

596 **References**

- 597 Alexander, M. J., Geller, M., McLandress, C., Polavarapu, S., Preusse, P., Sassi, F., Sato,
598 K., Eckermann, S., Ern, M., Hertzog, A., Kawatani, Y., Pulido, M., Shaw, T.A.,
599 Sigmond, M., Vincent, R. and Watanabe, S.: Recent developments in gravity-wave
600 effects in climate models and the global distribution of gravity-wave momentum
601 flux from observations and models, *Quarterly Journal of the Royal Meteorological*
602 *Society*, 136, 1103-1124, <https://doi.org/10.1002/qj.637>, 2010.
- 603 Alpert, J.: Sub-grid scale mountain blocking at NCEP, 20th Conference on Weather
604 Analysis and Forecasting/16th Conference on Numerical Weather Prediction,
605 https://ams.confex.com/ams/84Annual/techprogram/program_185.htm, 2004.
- 606 Beljaars, A. C. M., Brown, A. R., and Wood, N.: A new parametrization of turbulent
607 orographic form drag, *Quarterly Journal of the Royal Meteorological Society*, 130,
608 1327-1347, <https://doi.org/10.1256/qj.03.73>, 2004.
- 609 Booker, J. R., and Bretherton, F. P.: The critical layer for internal gravity waves in a shear
610 flow, *Journal of Fluid Mechanics*, 27, 513-539,
611 <https://doi.org/10.1017/S0022112067000515>, 1967.
- 612 Charney, J. G., and Drazin, P. G.: Propagation of planetary-scale disturbances from the
613 lower into the upper atmosphere, *Journal of Geophysical Research (1896-1977)*, 66,
614 83-109, <https://doi.org/10.1029/JZ066i001p00083>, 1961.
- 615 Chen, J., Ma, Z., Li, Z., Shen, X., Su, Y., Chen, Q., and Liu, Y.: Vertical diffusion and
616 cloud scheme coupling to the Charney-Phillips vertical grid in GRAPES global
617 forecast system, *Quarterly Journal of the Royal Meteorological Society*, 146, 2191-
618 2204, <https://doi.org/10.1002/qj.3787>, 2020.

- 619 Chen Q., Shen, X., Sun, J., and Liu, K.: Momentum budget diagnosis and the
620 parameterization of subgrid-scale orographic drag in global GRAPES, *Journal of*
621 *Meteorological Research*, 30, 771-788, [https://doi.org/10.1007/s13351-016-6033-](https://doi.org/10.1007/s13351-016-6033-y)
622 [y](https://doi.org/10.1007/s13351-016-6033-y), 2016.
- 623 Chen, P., and Robinson, W. A.: Propagation of Planetary Waves between the Troposphere
624 and Stratosphere, *Journal of Atmospheric Sciences*, 49, 2533-2545,
625 [https://doi.org/10.1175/1520-0469\(1992\)049<2533:POPWBT>2.0.CO;2](https://doi.org/10.1175/1520-0469(1992)049<2533:POPWBT>2.0.CO;2), 1992.
- 626 Choi, H. J., and Hong, S. Y.: An updated subgrid orographic parameterization for global
627 atmospheric forecast models, *Journal of Geophysical Research: Atmospheres*, 120,
628 12445-12457, <https://doi.org/10.1002/2015JD024230>, 2015.
- 629 Cohen, N. Y., Gerber, E. P., and Buhler, O.: Compensation between resolved and
630 unresolved wave driving in the stratosphere: Implications for downward control,
631 *Journal of the Atmospheric Sciences*, 70, 3780-3798, [https://doi.org/10.1175/JAS-](https://doi.org/10.1175/JAS-D-12-0346.1)
632 [D-12-0346.1](https://doi.org/10.1175/JAS-D-12-0346.1), 2013.
- 633 Dai, Y., Zeng, X., Robert, E. D., Baker, L., Bonan, G. B., Bosilovich, M. G., Denning A.
634 S., Dirmeyer, P. A., Houser, P. R., Niu, G., Oleson, K. W., Schlosser, C. A., Yang,
635 Z.: The Common Land Model, *Bulletin of the American Meteorological Society*,
636 84, 1013-1024, <https://doi.org/10.1175/BAMS-84-8-1013>, 2003.
- 637 Edmon, H. J., Hoskins, B. J. and McIntyre, M. E.: Eliassen-Palm Cross Sections for the
638 Troposphere, *Journal of Atmospheric Sciences*, 37, 2600-2616,
639 [https://doi.org/10.1175/1520-0469\(1980\)037<2600:EPCSFT>2.0.CO;2](https://doi.org/10.1175/1520-0469(1980)037<2600:EPCSFT>2.0.CO;2), 1980.

- 640 Fritts, D. C., and Alexander, M. J.: Gravity wave dynamics and effects in the middle
641 atmosphere, *Reviews of Geophysics*, 41, <https://doi.org/10.1029/2001RG000106>,
642 2003.
- 643 Han, J., and Pan, H. L.: Revision of Convection and Vertical Diffusion Schemes in the
644 NCEP Global Forecast System, *Weather and Forecasting*, 26, 520-533,
645 <https://doi.org/10.1175/WAF-D-10-05038.1>, 2011.
- 646 Haynes, P. H., McIntyre, M. E., Shepherd, T. G., Marks, C. J., and Shine, K. P.: On the
647 “Downward Control” of Extratropical Diabatic Circulations by Eddy-Induced
648 Mean Zonal Forces, *Journal of Atmospheric Sciences*, 48, 651-678,
649 [https://doi.org/10.1175/1520-0469\(1991\)048<0651:OTCOED>2.0.CO;2](https://doi.org/10.1175/1520-0469(1991)048<0651:OTCOED>2.0.CO;2), 1991.
- 650 Hersbach, H., Bell, B., Berrisford, P., et al: The ERA5 global reanalysis, *Quarterly Journal*
651 *of the Royal Meteorological Society*, 146, 1999-2049,
652 <https://doi.org/10.1002/qj.3803>, 2020.
- 653 Hong, S. Y., and Pan, H. L.: Nonlocal Boundary Layer Vertical Diffusion in a Medium-
654 Range Forecast Model, *Monthly Weather Review*, 124, 2322-2339,
655 [https://doi.org/10.1175/1520-0493\(1996\)124<2322:NBLVDI>2.0.CO;2](https://doi.org/10.1175/1520-0493(1996)124<2322:NBLVDI>2.0.CO;2), 1996.
- 656 Hu, D., Guo, Y., and Guan, Z.: Recent Weakening in the Stratospheric Planetary Wave
657 Intensity in Early Winter, *Geophysical Research Letters*, 46, 3953-3962,
658 <https://doi.org/10.1029/2019GL082113>, 2019.
- 659 Kim, Y. J.: Balance of drag between the middle and lower atmospheres in a global
660 atmospheric forecast model, *Journal of Geophysical Research: Atmospheres*, 112,
661 <https://doi.org/10.1029/2007JD008647>, 2007.

- 662 Kim, Y. J., and Arakawa, A.: Improvement of Orographic Gravity Wave Parameterization
663 Using a Mesoscale Gravity Wave Model, *Journal of Atmospheric Sciences*, 52,
664 1875-1902, [https://doi.org/10.1175/1520-
665 0469\(1995\)052<1875:IOOGWP>2.0.CO;2](https://doi.org/10.1175/1520-0469(1995)052<1875:IOOGWP>2.0.CO;2), 1995.
- 666 Kim, Y. J., and Doyle, J. D.: Extension of an orographic-drag parametrization scheme to
667 incorporate orographic anisotropy and flow blocking, *Quarterly Journal of the
668 Royal Meteorological Society*, 131, 1893-1921, <https://doi.org/10.1256/qj.04.160>,
669 2005.
- 670 Kim, Y. J., Eckermann, S., and Chun, H. Y.: An overview of the past, present and future
671 of gravity-wave drag parametrization for numerical climate and weather prediction
672 models - Survey article, *Atmosphere-ocean*, 41, 65-98,
673 <https://doi.org/10.3137/ao.410105>, 2003.
- 674 Klemp, J. B., and Durran, D. R.: An Upper Boundary Condition Permitting Internal Gravity
675 Wave Radiation in Numerical Mesoscale Models, *Monthly Weather Review*, 111,
676 430-444, [https://doi.org/10.1175/1520-0493\(1983\)111<0430:AUBCPI>2.0.CO;2](https://doi.org/10.1175/1520-0493(1983)111<0430:AUBCPI>2.0.CO;2),
677 1983.
- 678 Kruse, C. G., Smith, R. B., and Eckermann, S. D.: The Midlatitude Lower-Stratospheric
679 Mountain Wave “Valve Layer”, *Journal of the Atmospheric Sciences*, 73, 5081-
680 5100, <https://doi.org/10.1175/JAS-D-16-0173.1>, 2016.
- 681 Li, M., Xu, X., Teixeira, M. A. C., Xue, M., Xue, H., Zhu, K., and Huang, H.: Improved
682 Orographic Gravity Wave Drag Parameterization Accounting for the
683 Nonhydrostatic Effect in the Weather Research and Forecasting Model: Tests for

- 684 Short-Range Forecast of Northeast China Cold Vortices, *Monthly Weather Review*,
685 152, 2623-2637, <https://doi.org/10.1175/MWR-D-24-0097.1>, 2024.
- 686 Li, R., Xu, X., Xu, X., Shepherd, T. G., and Wang, Y.: Importance of orographic gravity
687 waves over the Tibetan Plateau on the spring rainfall in East Asia, *Science China*
688 *Earth Sciences*, 66, 2594-2602, <https://doi.org/10.1007/s11430-023-1204-6>, 2023.
- 689 Lindzen, R. S.: Turbulence and stress owing to gravity wave and tidal breakdown, *Journal*
690 *of Geophysical Research: Oceans*, 86, 9707-9714,
691 <https://doi.org/10.1029/JC086iC10p09707>, 1981.
- 692 Liu, K., Chen, Q., and Sun, J.: Modification of cumulus convection and planetary boundary
693 layer schemes in the GRAPES global model, *Journal of Meteorological Research*,
694 29, 806-822, <https://doi.org/10.1007/s13351-015-5043-5>, 2015.
- 695 Lott, F., and Miller, M. J.: A new subgrid-scale orographic drag parametrization: Its
696 formulation and testing, *Quarterly Journal of the Royal Meteorological Society*,
697 123, 101-127, <https://doi.org/10.1002/qj.49712353704>, 1997.
- 698 Lu, Y., Wu, T., Xu, X., Zhang, L., and Chu, M.: Improved Simulation of the Antarctic
699 Stratospheric Final Warming by Modifying the Orographic Gravity Wave
700 Parameterization in the Beijing Climate Center Atmospheric General Circulation
701 Model, *Atmosphere*, 11, 576, <https://doi.org/10.3390/atmos11060576>, 2020.
- 702 Lu, Y., Xu, X., Wang, L., Liu, Y., Wu, T., Jie, W., and Sun, J.: Machine Learning
703 Emulation of Subgrid-Scale Orographic Gravity Wave Drag in a General
704 Circulation Model with Middle Atmosphere Extension, *J. Adv. Model. Earth Syst.*,
705 16, e2023MS003611, <https://doi.org/10.1029/2023MS003611>, 2024.

- 706 Ma, Z., Liu, Q., Zhao, C., Shen, X., Wang, Y., Jiang, J. H., Zhe, L., and Yung, Y.:
707 Application and Evaluation of an Explicit Prognostic Cloud-Cover Scheme in
708 GRAPES Global Forecast System, *Journal of Advances in Modeling Earth Systems*,
709 10, 652-667, <https://doi.org/10.1002/2017MS001234>, 2018.
- 710 McFarlane, N. A.: The Effect of Orographically Excited Gravity Wave Drag on the General
711 Circulation of the Lower Stratosphere and Troposphere, *Journal of Atmospheric*
712 *Sciences*, 44, 1775-1800, [https://doi.org/10.1175/1520-](https://doi.org/10.1175/1520-0469(1987)044<1775:TEOOEG>2.0.CO;2)
713 [0469\(1987\)044<1775:TEOOEG>2.0.CO;2](https://doi.org/10.1175/1520-0469(1987)044<1775:TEOOEG>2.0.CO;2), 1987.
- 714 McLandress, C., Shepherd, T. G., Polavarapu, S., and Beagley, S. R.: Is Missing
715 Orographic Gravity Wave Drag near 60°S the Cause of the Stratospheric Zonal
716 Wind Biases in Chemistry-Climate Models? *Journal of the Atmospheric Sciences*,
717 69, 802-818, <https://doi.org/10.1175/JAS-D-11-0159.1>, 2012.
- 718 Miller, M. J., and Palmer, T. N.: Orographic gravity wave drag: Its parameterization and
719 influence in general circulation and numerical weather prediction models,
720 Presented at the ECWMF Workshop on Observation, Theory and Modelling of
721 Orographic Effects 1, 283-333, 1986.
- 722 Morcrette, J. J., Barker, H. W. J., Cole, N. S., Iacono, M. J., and Pincus, R.: Impact of a
723 New Radiation Package, McRad, in the ECMWF Integrated Forecasting System,
724 *Monthly Weather Review*, 136, 4773-4798,
725 <https://doi.org/10.1175/2008MWR2363.1>, 2008.
- 726 Palmer, T. N., Shutts, G. J., and Swinbank, R.: Alleviation of a systematic westerly bias in
727 general circulation and numerical weather prediction models through an orographic

- 728 gravity wave drag parametrization, *Quarterly Journal of the Royal Meteorological*
729 *Society*, 112, 1001-1039, <https://doi.org/10.1002/qj.49711247406>, 1986.
- 730 Scinocca, J., and McFarlane, N.: The parametrization of drag induced by stratified flow
731 over anisotropic orography, *Quarterly Journal of the Royal Meteorological Society*,
732 126, 2353-2393, <https://doi.org/10.1002/qj.49712656802>, 2000.
- 733 Shen, X., Su, Y., Hu, J., et al.: Development and Operation Transformation of GRAPES
734 Global Middle-range Forecast System, *Journal of Applied Meteorological Science*,
735 28, 1-10, <https://doi.org/10.11898/1001-7313.20170101>, 2017.
- 736 Shen, X., Wang, J., Li, Z., Chen, D., and Gong, J.: Research and operational development
737 of numerical weather prediction in China, *Journal of Meteorological Research*, 34,
738 675-698, <https://doi.org/10.1007/s13351-020-9847-6>, 2020.
- 739 Shen, X. S., Su, Y., Zhang, H. L., et al.: New version of the CMA-GFS dynamical core
740 based on the predictor-corrector time integration scheme, *Journal of Meteorological*
741 *Research*, 37, 273-285, <https://doi.org/10.1007/s13351-023-3002-0>, 2023.
- 742 Shutts, G.: Gravity-wave drag parametrization over complex terrain: The effect of critical-
743 level absorption in directional wind-shear, *Quarterly Journal of the Royal*
744 *Meteorological Society*, 121, 1005-1021, <https://doi.org/10.1002/qj.49712152504>,
745 1995.
- 746 Sigmond, M., and Shepherd, T. G.: Compensation between resolved wave driving and
747 parameterized orographic gravity wave driving of the Brewer-Dobson circulation
748 and its response to climate change, *Journal of Climate*, 27, 5601-5610,
749 <https://doi.org/10.1175/JCLI-D-13-00644.1>, 2014.

- 750 Smith, R. B.: The Influence of Mountains on the Atmosphere, In B. Saltzman (Ed.),
751 Advances in Geophysics (Vol. 21, pp. 87-230): Elsevier, 1979.
- 752 Teixeira, M. A. C.: The physics of orographic gravity wave drag, *Frontiers in Physics*, 2,
753 <https://doi.org/10.3389/fphy.2014.00043>, 2014.
- 754 van Niekerk, A., Vosper, S. B., and Teixeira, M. A. C.: Accounting for the three-
755 dimensional nature of mountain waves: Parametrising partial critical-level filtering,
756 *Quarterly Journal of the Royal Meteorological Society*, 149, 515-536,
757 <https://doi.org/10.1002/qj.4421>, 2023.
- 758 Wei, P., Xu, X., Xue, M., Li, J., Zhao, K., and Zhang, Q.: Complex Terrain Causes Global
759 Model Prediction Biases of 21.7 Zhengzhou Extreme Precipitation, *Science*
760 *Bulletin*, <https://doi.org/10.1016/j.scib.2025.09.015>, 2025.
- 761 Xu, X., Zhou, X., Yang, K., Lu, Y., Zhang, R., Yang, B., Tang, J., Wang, Y.: Reducing
762 Winter Precipitation Biases Over the Western Tibetan Plateau in the Model for
763 Prediction Across Scales (MPAS) With a Revised Parameterization of Orographic
764 Gravity Wave Drag, *Journal of Geophysical Research: Atmospheres*, 128,
765 e2023JD039123, <https://doi.org/10.1029/2023JD039123>, 2023.
- 766 Xu, X., Li, R., Teixeira, M. A. C., and Lu, Y.: On the Momentum Flux of Vertically
767 Propagating Orographic Gravity Waves Excited in Nonhydrostatic Flow over
768 Three-Dimensional Orography, *Journal of the Atmospheric Sciences*, 78, 1807-
769 1822, <https://doi.org/10.1175/JAS-D-20-0370.1>, 2021.
- 770 Xu, X., Teixeira, M. A. C., Xue, M., Lu, Y., and Tang, J.: Impacts of wind profile shear
771 and curvature on the parameterized orographic gravity wave stress in the Weather

- 772 Research and Forecasting model, Quarterly Journal of the Royal Meteorological
773 Society, 146, 3086-3100, <https://doi.org/10.1002/qj.3828>, 2020.
- 774 Xu, X., Wang, Y., and Xue, M.: Momentum Flux and Flux Divergence of Gravity Waves
775 in Directional Shear Flows over Three-Dimensional Mountains, Journal of the
776 Atmospheric Sciences, 69, 3733-3744, <https://doi.org/10.1175/JAS-D-12-044.1>,
777 2012.
- 778 Xu, X., Xue, M., Teixeira, M. A. C., Tang, J., and Wang, Y.: Parameterization of
779 Directional Absorption of Orographic Gravity Waves and Its Impact on the
780 Atmospheric General Circulation Simulated by the Weather Research and
781 Forecasting Model, Journal of the Atmospheric Sciences, 76, 3435-3453,
782 <https://doi.org/10.1175/JAS-D-18-0365.1>, 2019.
- 783 Xu, X., Zhang, R., Teixeira, M. A. C., van Niekerk, A., Xue, M., Lu, Y., Xue, H., Li, R.,
784 Wang, Y.: A Parameterization Scheme Accounting for Nonhydrostatic Effects on
785 the Momentum Flux of Vertically Propagating Orographic Gravity Waves:
786 Formulas and Preliminary Tests in the Model for Prediction Across Scales (MPAS),
787 Journal of the Atmospheric Sciences, 81, 805-817, <https://doi.org/10.1175/JAS-D-23-0020.1>, 2024.
- 789 Xue, H., Shen, X., and Su, Y.: Parameterization of Turbulent Orographic Form Drag and
790 Implementation in GRAPES, Journal of Applied Meteorological Science, 22, 169-
791 181, <http://qikan.camscma.cn/en/article/id/20110206>, 2011.
- 792 Zängl, G.: Orographic Gravity Waves Close to the Nonhydrostatic Limit of Vertical
793 Propagation, Journal of the Atmospheric Sciences, 60, 2045-2063,
794 [https://doi.org/10.1175/1520-0469\(2003\)060<2045:OGWCTT>2.0.CO;2](https://doi.org/10.1175/1520-0469(2003)060<2045:OGWCTT>2.0.CO;2), 2003.

- 795 Zhang, R.: CMA-GFS Model. Zenodo [code], <https://doi.org/10.5281/zenodo.18476721>,
796 2026.
- 797 Zhang, R.: CMA-GFS outputs. Zenodo [data set],
798 <https://doi.org/10.5281/zenodo.18529537>, 2026.
- 799 Zhang, R., Lu, Y., Xu, X., and Wang, Y.: Impacts of wind profile shear and curvature on
800 the parameterized orographic gravity wave stress in a middle atmosphere resolving
801 general circulation model, *Journal of Advances in Modeling Earth Systems*, 17,
802 e2024MS004232, <https://doi.org/10.1029/2024MS004232>, 2025.
- 803 Zhang, R., Xu, X., and Wang, Y.: Impacts of Subgrid Orographic Drag on the Summer
804 Monsoon Circulation and Precipitation in East Asia, *Journal of Geophysical*
805 *Research: Atmospheres*, 125, e2019JD032337,
806 <https://doi.org/10.1029/2019JD032337>, 2020.
- 807 Zhong, S., and Chen, Z.: Improved wind and precipitation forecasts over South China using
808 a modified orographic drag parameterization scheme, *Journal of Meteorological*
809 *Research*, 29, 132-143, <https://doi.org/10.1007/s13351-014-4934-1>, 2015.
810